1000 Days of the Lowest-frequency Emission from the Low-luminosity GRB 171205A

Barun Maity and Poonam Chandra
National Centre for Radio Astrophysics, TIFR, Pune University Campus, Post Bag 3, Pune 411 007, India; bmaity@ncra.tifr.res.in, poonam@ncra.tifr.res.in
Received 2020 April 24; revised 2020 November 30; accepted 2020 December 8; published 2021 January 29

Abstract

We report the lowest-frequency measurements of gamma-ray burst (GRB) 171205A with the upgraded Giant Metrewave Radio Telescope (uGMRT) covering a frequency range of 250–1450 MHz and a period of 4–937 days. It is the first GRB afterglow detected in the 250–500 MHz frequency range and the second brightest GRB detected with the uGMRT. Even though the GRB was observed for nearly 1000 days, there is no evidence of a transition to a nonrelativistic regime. We also analyzed the archival Chandra X-ray data on day ∼70 and day ∼200. We also found no evidence of a jet break from the analysis of combined data. We fit synchrotron afterglow emission arising from a relativistic, isotropic, self-similar deceleration as well as from a shock breakout of a wide-angle cocoon. Our data also allowed us to discern the nature and the density of the circumburst medium. We found that the density profile deviates from a standard constant density medium and suggests that the GRB exploded in a stratified wind-like medium. Our analysis shows that the lowest-frequency measurements covering the absorbed part of the light curves are critical to unraveling the GRB environment. Our data combined with other published measurements indicate that the radio afterglow has a contribution from two components: a weak, possibly slightly off-axis jet and a surrounding wider cocoon, consistent with the results of Izzo et al. The cocoon emission likely dominates at early epochs, whereas the jet starts to dominate at later epochs, resulting in flatter radio light curves.

Unified Astronomy Thesaurus concepts: Gamma-ray bursts (629); Gamma-ray transient sources (1853); Extragalactic radio sources (508)

1. Introduction

Gamma-ray bursts (GRBs) are the most energetic flashes of gamma-rays, with a T_{90} duration (time interval between which 5% and 95% of fluence is collected by the detector) ranging between a few milliseconds to thousands of seconds (Zhang 2019). The GRBs can be classified into two broad classes, i.e., short/hard GRBs with a duration of less than 2 s, and long/soft GRBs (LGRBs/SGRBs) with a duration greater than 2 s (Kouveliotou et al. 1993). According to well-accepted theories, most of long soft GRBs originate from the gravitational collapse of massive stars (collapsar model); and short hard GRBs result from explosive binary compact object mergers (Woosley & Bloom 2006). The GRBs from both channels of formation power relativistic collimated jets that give Doppler-boosted high luminosities in gamma-rays. GRBs are cosmological events with an average redshift of $z \approx 2.2$ (Fynbo et al. 2009), and have isotropic-equivalent gamma-ray luminosities ($L_{\rm iso}$) of the order of 10^{51}–10^{53} erg s^{-1}.

However, a handful of LGRBs/SGRBs with spectroscopically identified supernovae (SNe) have been discovered with luminosities that are 3–5 orders of magnitude lower than average, i.e., ($L_{\rm iso} \leqslant 10^{48.5}$ erg s^{-1}; Schulze et al. 2014; Cano et al. 2017b). Their low luminosities allow them to be detected only at low redshifts, though they may be 10–100 times more abundant than regular GRBs (Schmidt 2001). The prompt light curves of typical low-luminosity GRBs are smooth and their spectra have a single peak with the peak energy generally below ∼50 keV, which softens further with time (Nakar & Sari 2012; Cano et al. 2017b). The radio afterglow of these GRBs tend to indicate similar energy content in mildly relativistic ejecta (Kulkarni et al. 1998). Many of these GRBs are associated with broad-line Type Ic SNe. The list of such GRB SNe include some of the well-studied cases, such as GRB 980425/SN 1998bw ($z = 0.00866$, Galama et al. 1998),

GRB 030329/SN 2003dh ($z = 0.1685$, Hjorth et al. 2003), GRB 031203/SN 2003lw ($z = 0.1055$, Malesani et al. 2004), GRB 060218/SN 2006aj ($z = 0.0335$, Campana et al. 2006), GRB 100316D/SN 2010bh ($z = 0.0591$, Starling et al. 2011), GRB 111209A/SN 2011kl ($z = 0.677$, Gao et al. 2016), GRB 120422A/SN 2012bz ($z = 0.283$, Melandri et al. 2012), GRB 130427A/SN 2013cq ($z = 0.3399$, Melandri et al. 2014), GRB 130702A/SN 2013dx ($z = 0.145$, Cenko et al. 2013), GRB 161219B/SN 2016jca ($z = 0.1475$, Cano et al. 2017a), GRB 171010A/SN 2017htp ($z = 0.33$, Melandri et al. 2019), and GRB 190829A/ SN 2019oyu ($z = 0.08$, Terreran et al. 2019), although only five are nearby, $z \lesssim 0.1$ (Cano et al. 2017b, and references therein).

A significant amount of work has gone into understanding whether low-luminosity GRBs are simply the low-energy counterparts of the cosmological GRBs, or have a different emission mechanism. Many low-luminosity GRBs do not follow the $E_{\rm iso}-E_p$ Amati relation (Amati et al. 2002), indicating that their emission mechanism should be different from that of canonical, more distant GRBs. Technically an off-axis jet can also explain low-luminosity emission from GRBs, but predicts an achromatic steepening of the light curve, absent in many low-luminosity GRBs. There have been suggestions that in contrast to the emission from an ultra-relativistic jet driven by a central engine, these low-luminosity GRBs are powered by shock breakouts (SBOs; Kulkarni et al. 1998; Nakar & Sari 2012; Barniol Duran et al. 2015; Nakar 2015; Suzuki et al. 2017). In some cases observations have suggested a mildly relativistic blast wave being responsible for producing the radio afterglow. This has supported the relativistic SBO model, e.g., GRB 980425 (Kulkarni et al. 1998). The SBO model got further support in the of case of GRB 060218, in which a thermal component was also seen that cooled and shifted to optical/UV band with time. This was interpreted to

have arisen from the breakout of a shock driven by a mildly relativistic supernova (SN) shell in the progenitor wind (Campana et al. 2006), although late-time photospheric emission from a jet (Friis & Watson 2013), or thermal emission from a cocoon (Suzuki & Shigeyama 2013) can also explain it. Bromberg et al. (2011) have investigated whether low-luminosity GRBs launch relativistic jets like their high energy counterparts, but incur resistance by the stellar envelopes surrounding their progenitor stars. They found that some low-luminosity GRBs have much shorter durations compared to the jet breakout time. This is inconsistent with the collapsar model, which is largely successful in explaining the cosmological GRBs (Zhang 2019).

While Barniol Duran et al. (2015) and Nakar & Sari (2012) developed spherical relativistic SBO models in the context of low-luminosity GRBs, Nakar (2015) addressed some of the problems of the spherical SBO model by introducing a low-mass optically thick stellar envelope surrounding the progenitor star. In this model, the explosion powering the low-luminosity GRBs was not the spherical breakout of the SN shock, but was by a jet that gets choked in the envelope and powers a quasi-spherical explosion. To extend this idea further, Nakar & Piran (2017) considered a cocoon breakout model. In this model, as the GRB jet pushes through the stellar material, it heats the surrounding gas and produces a high-pressure sub-relativistic cocoon, which at the time of breakout, produces a relatively faint flare of gamma-rays. This breakout will not be as spherical as an SN breakout, but will be wider than a jet. In this model, the interaction of the cocoon with the surrounding medium can give rise to a late-time radio and X-ray afterglow. However, Irwin & Chevalier (2016) have provided an alternative mechanism, where the composite emission of GRB 060218/SN 2006aj could be explained by a weak jet, along with a quasi-spherical SN ejecta.

Low-luminosity GBRs also have a radio afterglow, which indicates a comparable energy in mildly relativistic ejecta (Kulkarni et al. 1998; Soderberg et al. 2004, 2006; Margutti et al. 2013). The lack of bright, late-time, radio emission from low-luminosity GRBs strongly constrain the total energy of any relativistic outflow involved in these events (Waxman 2004; Soderberg et al. 2004, 2006). Additionally, statistical arguments rule out the possibility that low-luminosity GRBs are regular LGRBs viewed at a large angle (e.g., Daigne & Mochkovitch 2007). Thus, if low-luminosity GRBs are generated by relativistic jets these jets must be weak and have a large opening angle. The bursts with $L_\gamma > 2 \times 10^{48}$ erg s^{-1} are considered as regular GRBs and are separated into LGRBs and SGRBs) according to the standard criterion of whether T_{90} in the observer frame is above or below 2 s (Bromberg et al. 2011).

GRB 171205A is a nearby low-luminosity GRB with a T_{90} duration of almost 189.4 s (D'Elia et al. 2018). It was first discovered by the Burst Alert Telescope onboard Swift on 2017 December 5 (D'Elia et al. 2017). It has a redshift of 0.0368 (D'Elia et al. 2017; Izzo et al. 2017). The isotropic energy release in gamma-ray band at the GRB rest frame was $2.18^{+0.63}_{-0.50} \times 10^{49}$ erg (D'Elia et al. 2018). The host of this event was a bright spiral galaxy named 2MASX J11093966-1235116 (Izzo et al. 2017), with a mass of the order of $10^{10} M_\odot$ and a star formation rate of $3 \pm 1 M_\odot$ yr^{-1} (Perley & Taggart 2017). An emergent SN event (SN 2017iuk) was seen 3 days after the burst (D'Elia et al. 2018).

There are a handful of observations for GRB 171205A from millimeter to radio bands. It was detected by de Ugarte Postigo et al. (2017) using the Northern Extended Millimeter Array with a flux density of ∼35 mJy at 150 GHz after 20.2 hr of the burst. The Atacama Large Millimeter/Submillimeter Array (ALMA) detected a bright afterglow of significance more than 100σ at 92 and 340 GHz on 2017 December 10 and 11 (Perley et al. 2017). The RATAN-600 radio telescope detected it at the 4.7 and 8.2 GHz bands during 2017 December 9–16 (Trushkin et al. 2017). The Karl G. Jansky Very Large Array (VLA) also observed the afterglow in the frequency range 4.5–16.5 GHz (Laskar et al. 2017). This GRB also had a Very Long Baseline Array detection at different frequencies (Perez-Torres et al. 2018). These observations showed a steeply rising spectrum ($\propto \nu^2$) at low frequency, which indicates a synchrotron self-absorbed spectrum. This is the first GRB for which Urata et al. (2019) claimed to have detected polarization at the ALMA 90 GHz frequency, though this claim has been disputed by Laskar et al. (2020). The upgraded Giant Metrewave Radio Telescope (uGMRT) first detected it on 2017 December 20 at 1400 MHz (Chandra et al. 2017a) after a non-detection on 2017 December 10 and 11 (Chandra et al. 2017b). The observed flux density at that epoch was 782 ± 57 μJy.

Radio afterglow emission from GRBs evolve slowly, which gives us the opportunity to observe it for a long time and obtain the distribution of the kinetic energy in the velocity space. Since this distribution is different for various models, especially central engine driven versus SBO, radio observations provide a unique opportunity to distinguish between various emission models (e.g., Kulkarni et al. 1998). Additionally, the early radio emission is likely to be absorbed via synchrotron self-absorption (SSA), and thus constrain the circumburst medium (CBM) density (Chandra et al. 2008). The late-time radio observations in the Newtonian limit, when the jet becomes sub-relativistic, are nearly independent of jet geometry and measure the kinetic energy of the afterglow accurately (Frail et al. 2000).

In this paper we present low-frequency observations of GRB 171205A taken with the uGMRT for around 1000 days. We summarize our observations and data analysis in Section 2. We discuss our model in Section 3.1 and our results in Section 3.2. In Section 4, we discuss the properties of GRB 171205A in conjunction with published measurements at higher frequencies and present our main conclusions. Unless otherwise stated, we assume a cosmology with $H_0 = 67.3$ km s^{-1} Mpc^{-1}, $\Omega_m = 0.315$, $\Omega_\Lambda = 0.685$ (Planck Collaboration et al. 2014).

2. Observation and Data Analysis

The GMRT observed GRB 171205A starting 2017 December 10 and continued observing until 2020 June 26. The observations were taken in Band 5 (1000–1450 MHz), Band 4 (550–900 MHz), and Band 3 (250–500 MHz). The bandwidth for Band 4 and Band 5 was 400 MHz, while for Band 3 it was 200 MHz. The duration of each observation was around 2–3 hr including overheads (on source time 1.5 hr). We observed flux density calibrators 3C286 and 3C48, and a phase calibrator J1130-148. Flux calibrators were also used as bandpass calibrators.

We use the package Common Astronomy Software Applications (CASA) for data analysis. The data were analyzed in three major steps, i.e., flagging, calibration, and imaging. The CASA task "flagdata" was used to remove dead antennas

Table 1
Flux Densities of GRB 171205A

Date of Observation	Band	Frequency (MHz)	Days since Explosion	Flux Density[a] (mJy)	Map rms (μJy/beam)
2017 Dec 10.10	5	1255	4.79	< 0.07	24
2017 Dec 11.02	4	648	5.71	<0.06	20
2017 Dec 19.91	5	1265	14.60	0.64 ± 0.05	17
2017 Dec 26.90	5	1265	21.59	1.00 ± 0.07	17
2017 Dec 28.91	4	607	23.60	<0.39	130
2018 Jan 16.94	5	1265	42.63	1.75 ± 0.05	17
2018 Feb 12.85	5	1370	68.54	3.04 ± 0.09	41
2018 Feb 17.85	4	607	73.54	1.37 ± 0.15	115
2018 Mar 20.68	5	1352	105.37	5.79 ± 0.08	34
2018 Jun 8.44	3	402	185.13	2.94 ± 0.41	106
2018 Jun 10.68	5	1255	187.37	3.07 ± 0.11	26
2018 Jun 11.42	4	745	188.11	2.46 ± 0.49	141
2018 Jul 13.47	5	1250	220.16	3.55 ± 0.12	17
2018 Jul 15.35	4	610	222.04	3.13 ± 0.18	66
2018 Jul 23.35	3	402	230.04	2.30 ± 0.22	64
2018 Jul 26.57	5	1265	233.26	2.60 ± 0.08	26
2018 Jul 28.35	4	750	235	2.92 ± 0.31	62
2018 Aug 24.32	5	1265	262.01	3.32 ± 0.06	33
2018 Aug 25.22	4	607	262.91	1.06 ± 0.16	81
2018 Sep 21.35	5	1265	290.04	3.03 ± 0.10	59
2018 Sep 23.16	3	402	291.85	2.01 ± 0.15	63
2018 Oct 20.28	5	1250	319	3.18 ± 0.13	52
2018 Oct 26.09	3	400	324.78	1.77 ± 0.27	131
2018 Oct 26.33	4	607	325.02	2.61 ± 0.26	143
2018 Dec 21.88	3	402	381.57	1.61 ± 0.31	49
2018 Dec 22.02	5	1255	381.71	2.83 ± 0.06	21
2018 Dec 22.14	4	610	381.83	1.52 ± 0.17	52
2019 Feb 26.98	4	610	448.67	1.52 ± 0.21	79
2019 Feb 26.70	3	402	448.39	1.05 ± 0.16	40
2019 Feb 26.87	5	1250	448.56	1.87 ± 0.06	17
2019 May 13.49	5	1250	524.18	1.74 ± 0.04	17
2019 May 13.62	3	402	524.31	1.43 ± 0.26	79
2019 May 13.77	4	607	524.46	2.09 ± 0.18	81
2019 Sep 10.16	5	1250	643.85	1.74 ± 0.03	19
2019 Sep 10.31	3	402	644.00	1.67 ± 0.21	50
2019 Sep 10.43	4	750	644.12	1.93 ± 0.10	30
2019 Dec 9.91	4	647	734.60	1.38 ± 0.12	37
2019 Dec 10.02	5	1265	734.71	1.71 ± 0.04	20
2019 Dec 10.19	3	402	734.88	1.30 ± 0.17	59
2020 Jun 26.37	4	648	934.06	1.29 ± 0.11	20
2020 Jun 26.49	5	1255	934.18	1.23 ± 0.04	21
2020 Jun 29.44	3	402	937.13	1.12 ± 0.16	55

Note.
[a] The uncertainties reflect the statistical errors.

and bad data. In addition, the tasks "tfcrop"[1] were used to flag radio frequency interference. The calibration (Taylor et al. 1999) was performed to remove the instrumental and atmospheric effects from the measurement. The final part of processing was imaging. The continuum imaging of the target source was done using CASA task "tclean." Finally, a few rounds of "phase only" mode and two rounds of "amplitude-phase" self-calibrations were run. We fit a Gaussian to determine the GRB flux density at the GRB position. The flux densities are shown in Table 1. Sample radio images of GRB 171205A at Bands 5, 4, and 3 are shown in Figure 1. The errors in flux densities in Table 1 show only the statistical errors. We also add 15% of flux densities in quadrature to account the

uncertainties due to calibration and other systematics for GMRT bands during our model fit. We closely follow the procedure shown in Chandra & Kanekar (2017). Table 1 list the details of our observations and flux densities at various epochs.

We also extract a Swift-XRT 0.3–10 keV flux light curve from the the Swift online repository (Evans et al. 2007).[2] The light curve post day 1 indicates a photon index of $\Gamma = 1.94^{+0.23}_{-0.22}$ and a column density of $N_H = (1.2^{+0.8}_{-0.7} \times 10^{21}$ cm^{-2}.[3] This is in addition to a Galactic column density of 5.89×10^{20} cm^{-2}. We converted X-ray flux into 1 keV spectral flux density using this photon index. Swift data covered observations until 2020 May 27.

---

[1] http://www.aoc.nrao.edu/~rurvashi/TFCrop/TFCropV1/node2.html and "rflag" https://casa.nrao.edu/Release4.2.2/docs/userman/UserMansu167.html

[2] https://www.swift.ac.uk/xrt_products/00794972
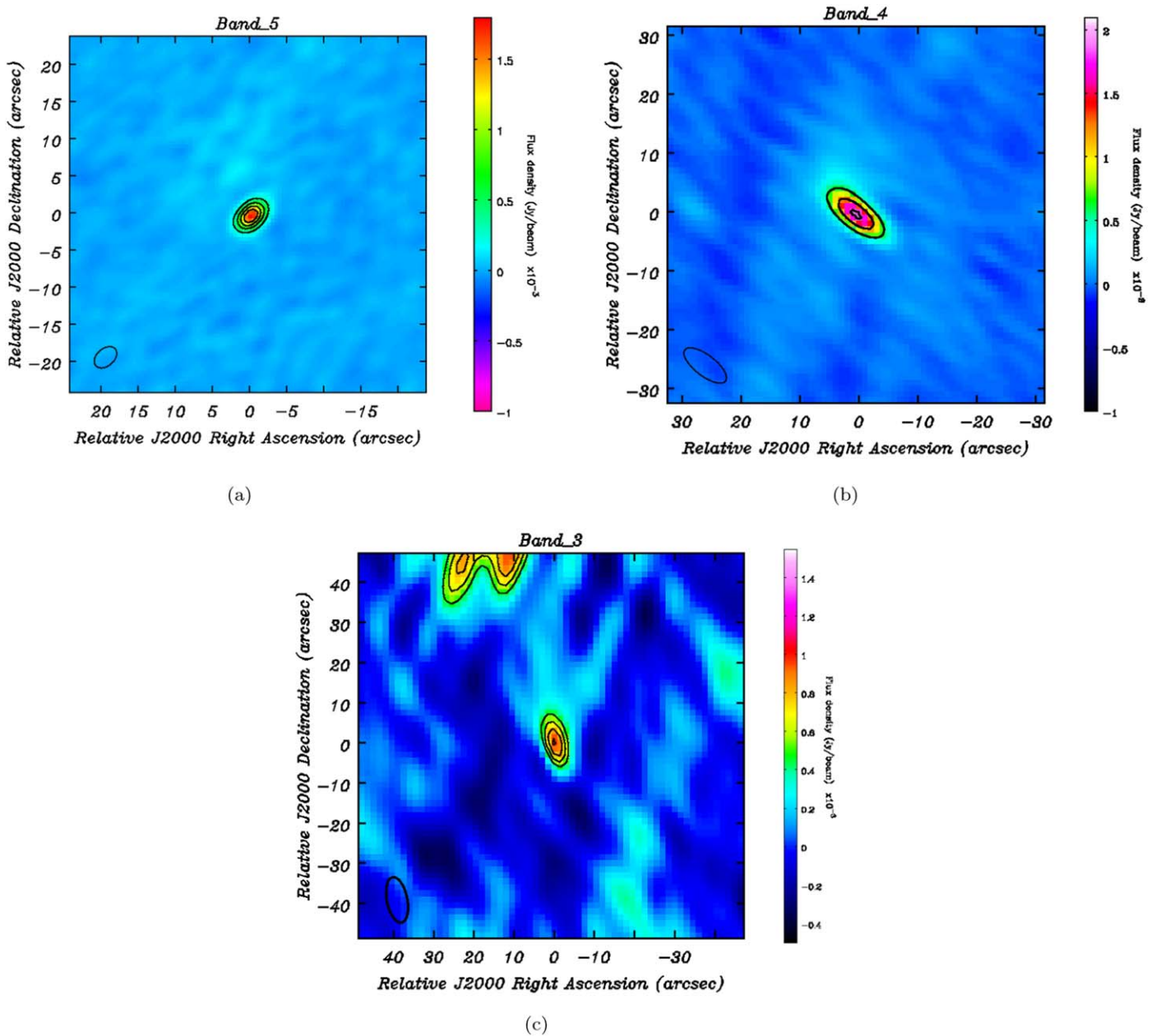[3] https://www.swift.ac.uk/xrt_live_cat/00794972/

Figure 1. GMRT images of GRB 171205A. Panel (a) Band 5 detection on 2019 May 13. Panel (b) Band 4 detection on 2019 September 10. Panel (c) Band 3 detection on 2019 May 13. The contours in black lines show the detection significance and are at 20, 40 and 60σ for Bands 4 and 5, and at 6, 8, and 10σ for Band 3, where σ is the map rms of the corresponding images. For the images displayed, they are following: Band 5, 17 μJy, Band 4, 30 μJy, and Band 5, 80 μJy.

In addition, we analyzed two archival data from Chandra ACIS-S on 2018 February 14 and 2018 June 29 (PI: Margutti). We used the Chandra Interactive Analysis of Observations software (CIAO; Fruscione et al. 2006) task specextrac-tor to extract the spectra, response and ancillary matrices. We used CIAO version 4.6 along with CalDB version 4.5.9. The HEAsoft[4] package Xspec version 12.1 (Arnaud 1996) was used to carry out the analysis of the Chandra spectra. The GRB was detected in the first observations at 71 days with 0.3–10 keV of unabsorbed flux of $(11.25 \pm 3.38) \times 10^{-15}$ erg cm^{-2} s^{-1}. The second Chandra observation on the second epoch, i.e., 206 days, resulted in a 3σ upper limit $<3.98 \times 10^{-15}$ erg cm^{-2} s^{-1}.

3. Modeling and Results

3.1. GRB Afterglow (AG) Model

We used the external synchrotron model for the GRB afterglow emission, which arises due to the interaction between the GRB outflow and the surrounding CBM (Granot & Sari 2002). As the outflow moves into the CBM, a "forward shock" or a "blast wave" shock moving into the CBM, and a "reverse shock" moving into the ejected outflow are created. These shocks have the ability to accelerate charged particles to relativistic speeds via Fermi acceleration (Longair 2011). Radio afterglow emission is expected to be synchrotron emission arising due to these relativistic charged particles in the shocks in the presence of magnetic fields.

The evolution of the blast wave is "self-similar" (Blandford & McKee 1976), and the dynamics depends only on the density of the CBM and the blast wave energy. The CBM is usually modeled to be one of the two forms, a constant density medium and a wind-like density medium (Chevalier & Li 2000). The number density profile of the ambient medium is usually modeled as a power law $n \propto r^{-k}$. For the constant density case, the parameter $k = 0$ and $n = n_0$. For the wind-like case, the mass flows radially outwards at uniform speed and rate from the GRB progenitor giving $k = 2$; hence, for a mass-loss rate from the progenitor $\dot{M}_W$ and the progenitor wind velocity V_W, the density can be defined as (Chevalier et al. 2004; Gao et al. 2013)

$$n = \frac{\dot{M}_W}{4\pi r^2 m_p V_W} = 3 \times 10^{35} A_* r^{-2}, \quad (1)$$

where m_p is the mass of the proton, A_* is in units of 3×10^{35} cm^{-1} (or 5×10^{11} g cm^{-1} for the mass density), corresponding to $\dot{M}_{W,-5}/V_{W,3}$. Here $\dot{M}_{W,-5}$ is the mass-loss rate in $10^{-5} M_\odot$ yr^{-1} and $V_{W,3} = 10^3$ km s^{-1}.

The GRB wideband afterglow spectrum has several breaks characterized by various characteristic frequencies, namely, ν_a (the transition from the optically thick to the thin region, i.e., SSA peak), ν_c (synchrotron cooling frequency) and ν_m (frequency corresponding to the minimum injected Lorentz factor). In the fast cooling regime the frequency ordering is $\nu_m > \nu_c$, while in the slow cooling regime the ordering is the opposite. Generally, afterglow modeling is done in the slow cooling regime, where the most relevant ordering in radio frequencies in first few days are $\nu_a \lesssim \nu_m \lesssim \nu_c$, and then $\nu_m \lesssim \nu_a \lesssim \nu_c$ at later times (Granot & van der Horst 2014). However, there has been evidence for fast cooling in some GRBs with high density environments (Chandra et al. 2008). The afterglow spectra evolves as $F_\nu \propto \nu^2$ ($\nu < \nu_a$) and $F_\nu \propto \nu^{1/3}$ ($\nu_a < \nu < \min(\nu_m, \nu_c)$) for both the fast as well as the slow cooling regimes. In the regime of $\min(\nu_m, \nu_c) < \nu < \max(\nu_m, \nu_c)$, the evolution changes to $F_\nu \propto \nu^{-1/2}$ and $F_\nu \propto \nu^{-(p-1)/2}$ for the fast and slow cooling regimes, respectively, and then evolves as $F_\nu \propto \nu^{-p/2}$ for $\nu > \max(\nu_m, \nu_c)$, where p is the usual power-law index showing particle number distribution with energy in the nonthermal emission case.

In addition to standard AG models, the SBO model also has been favored for low-luminosity GRBs, where the breakout of a shock traveling through the stellar envelope may be responsible for gamma-ray emission. Due to the decreasing density of the stellar matter outwards, the SBO velocity increases and may become relativistic. Nakar & Sari (2012) have defined a "relativistic breakout closure relation" between the breakout energy E_{bo}, temperature T_{bo}, and duration t_{bo}^{obs}, i.e., $(t_{bo}^{obs}/20 \text{ s}) \sim (E_{bo}/10^{46} \text{ erg})^{1/2}(T_{bo}/50 \text{ keV})^{-2.68}$. This relation has been found to be followed by several low-luminosity GRBs. For GRB 171205A, the relation gives ~ 80 s, which is roughly one-third of the observed duration. However, the large uncertainties in the E_p and E_{iso} (D'Elia et al. 2018) do not rule out this model.

3.2. Inputs from High Frequency Data

The Swift-XRT light curve covers the epoch until day ~ 902. In addition, Chandra observations are on day 71 and day 205 (Figure 2). We fit a power law to the X-ray data post day 1. This is to avoid possible energy injection due to central engine
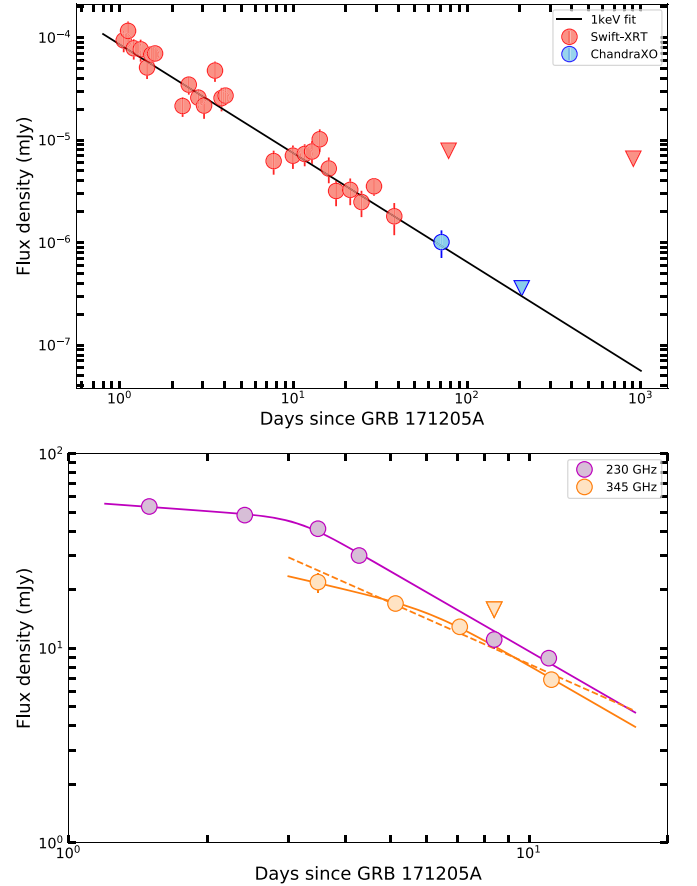

Figure 2. Top panel: the 1 keV X-ray light curve of GRB 171205A from day 1 onwards. Swift-XRT data points are in red and Chandra data points are in blue. The triangle symbol indicates the 3σ upper limit. The light curve is best fit with a power law with an index of -1.06 ± 0.06. Bottom panel: early time 230 and 345 GHz light curves GRB 171205A. The values are taken from Urata et al. (2019). The light curves are jointly fit with a broken power law with a common post-peak index (solid lines). In addition, we also fit the 345 GHz light curve with a simple power-law model to determine the significance of the break.

activities at $\leqslant 1$ day. The light curve is fit with the power-law index $\alpha = 1.06 \pm 0.06$. D'Elia et al. (2018) also found a power-law fit with an index of 1.08 to the light curve post ~ 1 day, consistent with our value. This is the typical value for the standard X-ray light-curve decay before jet break (Panaitescu & Kumar 2002), suggesting that no jet break was seen until the last Swift-XRT epoch. The jet break time is thus constrained to $t_{jet} \geqslant 71$ days (Rhoads 1999), i.e., the last detected Chandra epoch.

The photon index of the Swift-XRT data is a photon index $\Gamma = 1.94^{+0.23}_{-0.22}$ (see footnote 2). This suggests $\beta = 0.94^{+0.23}_{-0.22}$. The values of α and β are consistent with the X-ray frequency (ν_X) being above the cooling frequency ($\nu_X > \nu_c$), for both wind as well as the interstellar medium (ISM) density profiles. The X-ray temporal index is consistent with $\alpha = (3p-2)/4$ and spectral index $\beta = p/2$. These values make $p = 2.08 \pm 0.08$ and 1.88 ± 0.46, respectively, which within the error bars, are consistent with each other. Within the error bars, this is also consistent with $\nu_X < \nu_c$ for an ISM-like medium, where $\alpha = 3(p-1)/4$ and $\beta = (p-1)/2$.

We also plot early time 230 and 345 GHz light curves GRB 171205A, taken from Urata et al. (2019). We estimate the realistic error bars in the flux density values by adding 5% of
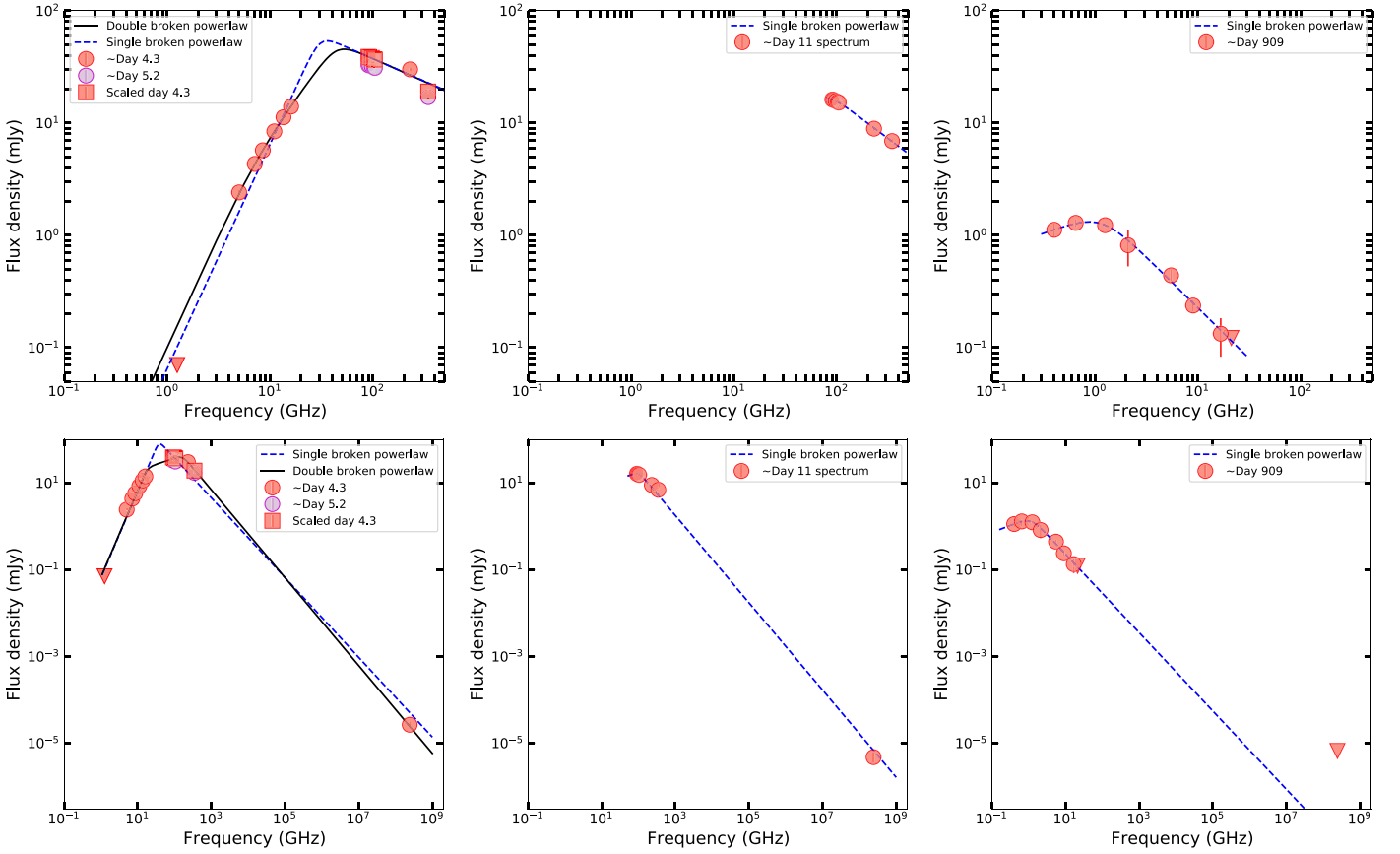
Figure 3. Top panel: near-simultaneous spectra on day ∼4, day ∼11, and day ∼909. Here we use only the centimeter and millimeter data. Bottom panel: the same as the top panel but including the X-ray data as well. The spectra are fit with single SBPL fits. For day 4.2, we also fit the data with a power law with two breaks. The DBPL fit is indicated with a black continuous line and the single one with a dashed blue line.

the flux density in quadrature to the map rms to account for the systematic errors. The millimeter highest flux density is significantly higher than the peak flux densities at the uGMRT bands, indicating most likely the presence of a wind-like medium. The millimeter light curves are jointly fit with a broken power law with a common post-peak index. The data are best fit with post-break index of -1.37 ± 0.07 (bottom panel of Figure 2). For the above values of p, this is consistent with an evolution of $(3p-1)/4$, for $\nu_m < \nu_{mm} < \nu_c$ for the wind density profile. The pre-break indices -0.17 ± 0.14 and -0.54 ± 0.31 for the 230 and 345 GHz bands, respectively. The breaks in 230 and 345 GHz are at 3.14 ± 0.28 day and 6.12 ± 1.17 day, respectively. At the epochs of the breaks, the flux density of the 230 and 345 GHz light curves are 43.83 ± 3.29 and 14.85 ± 2.86 mJy, respectively. We also fit the 345 GHz data with a single power-law model to determine the significance of the break. The single power-law model fits with an index of -1.05 ± 0.14, however, this results in a much larger reduced-χ^2 value of 2.47 as compared to 0.81 in the broken power-law case. For the broken power-law model, the characteristic frequency evolves with an index of $+0.71 \pm 0.12$, hence, the breaks cannot be due to passage of ν_m, which decreases with time. The only possibility is the breaks are due to ν_c in the wind medium, where $\nu_c \propto t^{1/2}$. Thus, the data indicate $\nu_c \approx 230$ GHz on day 3.14 and $\nu_c \approx 345$ GHz on day 6.12. However, there is one concern. The pre-break evolution is rather flat. This could be reconciled if millimeter bands are close to the passage of ν_m. Another possibility is that there is a reverse shock component that is contributing to the

millimeter band at the early epoch. The thick shell reverse shock model during the reverse shock crossing phase will evolve as $-(p-2)/2$, for $\nu_{mm} > \nu_c$ in the slow cooling phase and $\nu_{mm} > \nu_m$ in the fast cooling phase. The characteristic frequency evolves with an index of $+0.71 \pm 0.12$; this is in between the evolution of the ν_c ($\propto t^{1/2}$) in the forward shock and the evolution of ν_c ($\propto t^1$) in the reverse shock. This also suggests the possibility of reverse shock contributing to the AG model. If so, then the breaks at days 3.14 and 6.12 in 230 and 345 GHz are artificial breaks and may not reflect the cooling break.

We also combined the early epoch published centimeter and millimeter data from Urata et al. (2019), and late epoch Australian Telescope Compact Array data from Leung et al. (2020) with the uGMRT and the X-ray data, to obtain near-simultaneous spectra on around day 4, day 11, and day 909 (Figure 3). For the early epoch spectrum, the VLA data are on day 4.3 and the ALMA data are on day 5.2. We use the nearest epoch temporal evolution to derive the ALMA values on day 4.3. In the figure, we plot the values on day 5.2 as well as their derived values on day 4.3 along with the VLA data. We do not use optical data as SN signatures appeared by day 3 and hence the optical data are likely to be heavily contaminated by the underlying SN. We fit smooth single broken power-law (SBPL) and smooth double broken power-law (DBPL) fits to day 4.3 spectrum. We used the formalism of Granot & Sari (2002) for the treatment of smoothing of power laws at the break frequencies. We first fit only the centimeter and millimeter data. For day 4.3, the best-fit SBPL model peaks at 30.41 ± 4.08 GHz

and afterwards evolves as -0.41 ± 0.25. Here we have fixed the pre-break spectral index to 2. However, even when we use this as a free parameter, the best-fit index is consistent with 2 within error bars. The DBPL model fits the data well and give the breaks at 7.25 ± 2.11 GHz and 44.41 ± 3.62 GHz with post-break indices 1.26 ± 0.12, and -0.41 ± 0.02, respectively. The peak flux density is 43.80 ± 1.12 mJy.

We also fit the SBPL for the spectrum on day 11 and 909. The data indicates a fit -0.68 ± 0.02 with a peak of < 90 GHz, with the peak flux density of > 16.2 mJy. The pre-break index is 0.43 ± 0.46. The spectra on day 909 are fit with pre-break and post-break indices of 0.15 ± 0.13 and -0.90 ± 0.04, respectively, and a peak at 1.55 ± 0.48 GHz. The peak flux at day 909 is 1.15 ± 0.16 mJy.

Now we carry out the above fits including the X-ray data as well. The data to millimeter to X-ray data are fit by indices close to -1. These values are -1.01 ± 0.18 and -1.01 ± 0.02 for the first two spectra, respectively. For day 909, the X-ray upper limit does not constrain the model. The millimeter to X-ray indices consistent with the X-ray spectral indices are between 0.3 and 10 keV. This indicates that the cooling frequency (ν_c) is probably close to millimeter values if $\nu_X > \nu_c$. Due to lack of optical data, we were unable to constrain the cooling frequencies more precisely.

The peak flux density and the frequency of the peak in the three cases are 37.79 ± 3.95 mJy at 160.93 ± 35.31 GHz, > 16.2 mJy at < 90 GHz, and 1.15 ± 0.16 mJy at 1.55 ± 0.48 GHz, respectively. Our analysis indicates that the peak of the spectra on day 4 and day 909 are due to ν_m or ν_a. Between day 4 and 909, the peak flux density evolves as -0.63 ± 0.02. This clearly rules out an ISM model and supports the wind model.

Zhang et al. (2007) estimated kinetic energy in the synchrotron afterglow, E_K, from the X-ray data at the time of shallow to normal decay, which for GRB 171205A is 1.05 day. For $\nu_X > \nu_c$, E_K is independent of density and is only weakly depends on B and p, and therefore is an ideal regime to measure E_K. One can then derive E_K from the X-ray band using Equation (9) of Zhang et al. (2007), which in this case is $E_K \approx 1.4 \times 10^{50} (\epsilon_B/0.01)^{2-p/2 + p} (\epsilon_e/0.1)^{4(1-p)/2+p}$ erg.

3.3. Initial Inferences from uGMRT Data

We plot uGMRT radio light curves and fit them jointly with an SBPL model. We allow the normalization to vary but fix the indices before and after the peak. We show the light curves in Figure 4. In the figure, the Band 4 and 5 values are scaled by factors of 10 and 100, respectively, for clarity. The indices before and after the peak are 1.37 ± 0.20 and -0.72 ± 0.06.

The evolution before peak at uGMRT frequencies (ν_{radio}) is in rough agreement with the wind slow cooling phase for $\nu_{radio} < \nu_a$ for $\nu_a < \min(\nu_m, \nu_c)$; the wind fast cooling phase for $\nu_a < \nu_c < \nu_m$ if the observing frequency is in the transition zone between $\nu_{radio} < \nu_a$ to $\nu_a < \nu_{radio} < \nu_c$, as well as the wind slow cooling phase for $\nu_m < \nu_a < \nu_c$ for the transition between $\nu_{radio} < \nu_m$ to $\nu_m < \nu_{radio} < \nu_a$. The post-peak index is rather shallow and is consistent only with the wind fast cooling phase in the regime of $\nu_a < \nu_{radio} < \nu_c$. It is rather shallow for the post-jet break or nonrelativistic evolution. However, as we discuss in the next section, the shallow decline of the radio light curve is seen in other GRBs as well, and other emission components may contribute to it.

From our fits, the epochs of the peak flux densities are 5.19 ± 0.05 and 3.23 ± 0.15 mJy, respectively, in Bands 5 and
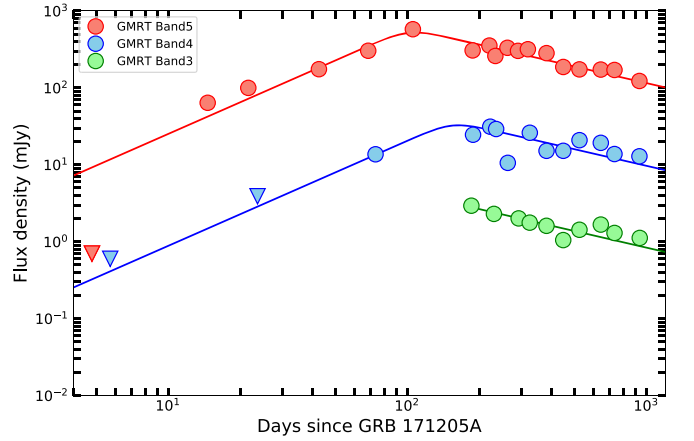

Figure 4. The uGMRT Bands 5, 4, and 3 radio light curves (the Band 4 and 5 values are scaled by factors of 10 and 100). The data are best fit with pre- and post-peak spectral indices of 1.37 ± 0.20 and -0.72 ± 0.06.

4 on day 101.08 ± 9.58 and day 153.71 ± 40.31, respectively. In Band 3, the data are optically thin, which constrains the peak to be < 185.13 day and flux > 2.81 mJy. The peak flux density evolves as -1.13 ± 0.76. While this value has a large error, it is consistent with the evolution in the stratified wind within 2σ and most likely rules out all the models involving ISM, where $F_{max} \propto t^0$. This also rules out the $1 < p < 2$ case for which $F_{\nu,max}$ is expected to remain constant (Gao et al. 2013).

3.4. Model Fits

In this section, we carry out detailed model fits to the uGMRT data. The simple closure relations seem to suggest that the GRB is in a slow cooling regime for the wind density medium. We fit the data with all three scenarios, i.e., the wind density slow cooling regime $\nu_a < \nu_m < \nu_c$, $\nu_m < \nu_a < \nu_c$, and the wind density fast cooling regime $\nu_a < \nu_c < \nu_m$. We also account for the nonstandard wind profile, i.e., $k \neq 2$. For this we keep k as a free parameter and adopt the expressions shown in van der Horst (2007).

Models are proposed for different stages of blast wave expansion. The precise coefficients associated with specified model parameters can be computed by numerical simulations. For the decelerating blast wave and the adiabatic wind-like case the parameter dependencies of the peak flux density and characteristic frequencies are given by Gao et al. (2013)

$$F_{\nu,max} = 17.0 \text{ mJy} \left(\frac{1+z}{2}\right)^{3/2} \left(\frac{E_{KE}}{10^{49} \text{ erg}}\right)^{1/2} \left(\frac{\epsilon_B}{0.01}\right)^{1/2}$$
$$\left(\frac{A_*}{0.1 \dot{M}_{W,-5}/V_{W,3}}\right) \left(\frac{D}{100 \text{ Mpc}}\right)^{-2} \left(\frac{t}{10 \text{ days}}\right)^{-1/2}, \tag{2}$$

$$\nu_c = 1.7 \times 10^{17} \text{ Hz} \left(\frac{1+z}{2}\right)^{-3/2} \left(\frac{E_{KE}}{10^{49} \text{ erg}}\right)^{1/2}$$
$$\left(\frac{A_*}{0.1 \dot{M}_{W,-5}/V_{W,3}}\right)^{-2} \left(\frac{\epsilon_B}{0.01}\right)^{-3/2} \left(\frac{t}{10 \text{ days}}\right)^{1/2}, \tag{3}$$

$$\nu_m = 2.7 \times 10^7 \text{ Hz } G'(p) \left(\frac{1+z}{2}\right)^{1/2} \left(\frac{E_{KE}}{10^{49} \text{ erg}}\right)^{1/2}$$

$$\left(\frac{\epsilon_e}{0.1}\right)^2 \left(\frac{\epsilon_B}{0.01}\right)^{1/2} \left(\frac{t}{10 \text{ days}}\right)^{-3/2}, \quad (4)$$

where the parameters ϵ_B and ϵ_e are microscopic parameters indicating the fraction of energy into the magnetic field and relativistic electrons, respectively, and E_{KE} is the afterglow kinetic energy, $G'(p) = 0.053((p-2)/(p-1))^2$.

The expression ν_a for the three regimes are

$$\nu_a \begin{cases} = 4.3 \times 10^9 \text{ Hz } g'(p) \left(\frac{1+z}{2}\right)^{-2/5} \left(\frac{E_{KE}}{10^{49} \text{ erg}}\right)^{-2/5} \\ \left(\frac{A_*}{0.1 \dot{M}_{W,-5}/V_{W,3}}\right)^{6/5} \left(\frac{\epsilon_B}{0.01}\right)^{1/5} \left(\frac{\epsilon_e}{0.1}\right)^{-1} \left(\frac{t}{10 \text{ days}}\right)^{-3/5}, \\ \quad \text{for } \nu_a < \nu_m < \nu_c. \\ = 4.9 \times 10^8 \text{ Hz } g''(p) \left(\frac{1+z}{2}\right)^{\frac{p-2}{2(p+4)}} \left(\frac{E_{KE}}{10^{49} \text{ erg}}\right)^{\frac{p-2}{2(p+4)}} \\ \left(\frac{A_*}{0.1 \dot{M}_{W,-5}/V_{W,3}}\right)^{\frac{4}{p+4}} \left(\frac{\epsilon_B}{0.01}\right)^{\frac{p+2}{2(p+4)}} \left(\frac{\epsilon_e}{0.1}\right)^{\frac{2(p-1)}{p+4}} \left(\frac{t}{10 \text{ days}}\right)^{-\frac{3(p+2)}{2(p+4)}}, \\ \quad \text{for } \nu_m < \nu_a < \nu_c. \\ = 6.0 \times 10^4 \text{ Hz } g'''(p) \left(\frac{1+z}{2}\right)^{3/5} \left(\frac{E_{KE}}{10^{49} \text{ erg}}\right)^{-2/5} \\ \left(\frac{A_*}{0.1 \dot{M}_{W,-5}/V_{W,3}}\right)^{11/5} \left(\frac{\epsilon_B}{0.01}\right)^{6/5} \left(\frac{t}{10 \text{ days}}\right)^{-8/5}, \\ \quad \text{for } \nu_a < \nu_c < \nu_m. \end{cases} \quad (5)$$

where the expressions for $g'(p)$, $g''(p)$, and $g'''(p)$ are derived in Gao et al. (2013) and for $p = 2.1$. Using these expressions, the temporal and spectral evolution in different transitions regimes can be derived and are mentioned in Gao et al. (2013).

We also carry out modeling for the SBO cases, for which we adopt the methodology of Barniol Duran et al. (2015). In this model, due to decreasing outer ejecta density, the outer parts of the shock envelope are faster and less energetic, and the inner parts are slower and more energetic. As slower material catches up with the decelerating ejecta it reenergizes the forward shock and the blast wave energy continuously changes with time. Thus, this model can be treated as a series of successive shells that accelerate and catch up to the boundary and hence explain the increasing afterglow energy via continuous injection (Barniol Duran et al. 2015). If η is the ratio of the prompt to afterglow energy ($\eta \equiv E_{\gamma.\text{iso}}/E_{k,\text{iso}}$), then for the SBO case, we parameterize the model as $\eta_{\text{eff}} E_{k,\text{iso}} = E_{\gamma.\text{iso}} \left(\frac{tA_*}{1+z}\right)^s$, where s is a free parameter characterizing energy injection (Barniol Duran et al. 2015).

Using this expression along with the scalings for ν_a, ν_m, ν_c, and $F_{\max}$ for various regimes, provided by Barniol Duran et al. (2015), leads to the following closure relations for a wind-like medium:

Case 1 ($\nu_a < \nu_m < \nu_c$):

$$F_\nu(t) \propto \begin{cases} \nu^2 t^{s+1}, & \text{for } \nu < \nu_a \\ \nu^{1/3} t^{\frac{s}{3}}, & \text{for } \nu_a < \nu < \nu_m \\ \nu^{-(p-1)/2} t^{-\frac{3p-1-s(p+1)}{4}}, & \text{for } \nu_m < \nu < \nu_c \\ \nu^{-p/2} t^{-\frac{3p-2-s(p+2)}{4}}, & \text{for } \nu > \nu_c \end{cases} \quad (6)$$

Case 2 ($\nu_m < \nu_a < \nu_c$):

$$F_\nu(t) \propto \begin{cases} \nu^2 t^{s+1}, & \text{for } \nu < \nu_m \\ \nu^{5/2} t^{\frac{7+3s}{4}}, & \text{for } \nu_m < \nu < \nu_a \\ \nu^{-(p-1)/2} t^{-\frac{3p-1-s(p+1)}{4}}, & \text{for } \nu_a < \nu < \nu_c \\ \nu^{-p/2} t^{-\frac{3p-2-s(p+2)}{4}}, & \text{for } \nu > \nu_c \end{cases} \quad (7)$$

Case 3 ($\nu_a < \nu_c < \nu_m$):

$$F_\nu(t) \propto \begin{cases} \nu^2 t^{2+s}, & \text{for } \nu < \nu_a \\ \nu^{1/3} t^{-\frac{2(s+1)}{3}}, & \text{for } \nu_a < \nu < \nu_c \\ \nu^{-1/2} t^{-\frac{s+1}{4}}, & \text{for } \nu_c < \nu < \nu_m \\ \nu^{-p/2} t^{-\frac{3p-2+(p+2)s}{4}}, & \text{for } \nu > \nu_m. \end{cases} \quad (8)$$

We now fit the uGMRT data with both the standard isotropic afterglow and SBO AG models. We use SBPL models for various regimes following the procedure in Granot & Sari (2002). We use $z = 0.036$ and $D = 163$ Mpc. We define $E_{KE} = E_{\gamma.\text{iso}}/\eta$, and keep η (η_{eff} for SBO) as the free parameter. The parameters p, A_*, ϵ_B, and ϵ_e are also free parameters.

With the inputs above, we carry out the detailed modeling using Markov chain Monte Carlo fitting using the Python package emcee (Foreman-Mackey et al. 2013). We choose 150 walkers and 2000 steps. Even though the analytical modeling suggests a wind-like medium, we start with fits to a constant density medium. The fit results in a high values of reduced χ^2 further ruling out the constant density model. We fit the standard wind model with $k = 2$ for all the cases. In addition, we also account for a nonstandard wind density medium keeping k as a free parameter.

Table 2 shows the fit statistics for different parameters using the above-mentioned models. For the $\nu_a < \nu_m < \nu_c$ case, we do not list the general k model as this model performed quite poorly for both afterglow as well as SBO. $\nu_a < \nu_m < \nu_c$ generally performs very poorly, with the SBO model performing slightly better than the isotropic AG model. In addition, the parameters obtained in this model are rather unphysical. While the fast cooling model gives best reduced χ_ν^2, this case is unlikely to be true. The analysis of millimeter and X-ray light published data have already revealed that ν_c lies between the millimeter and X-ray frequencies. Since $\nu_c \propto t^{1/2}$ in the wind model, uGMRT radio frequencies cannot be in the fast cooling regime.

The most viable model fits are obtained for the $\nu_m < \nu_a < \nu_c$ case. This is quite viable since in the wind density profile, ν_m evolves faster than ν_a and may reach the $\nu_m < \nu_a$ regime at late epochs (Granot & van der Horst 2014). Here keeping k as free parameter also results in $k \sim 2$. Our model fits are equally good for the standard AG model and the SBO model, and uGMRT data alone cannot differentiate between the two.

In Figure 5, we show the light curve for a standard wind $k = 2$ model for the $\nu_m < \nu_a < \nu_c$ case for both isotropic forward shock afterglow as well as the SBO AG model.

4. Discussion

4.1. Properties of GRB 171205A from Radio Modeling

The peak radio flux density of GRB 171205A at 1.3 GHz is $\sim 10^{29}$ erg s^{-1} Hz^{-1}. This is two orders of magnitude fainter

Table 2
Best-fit Parameters for the GRB 171205A uGMRT Data

Parameter	$\nu_a < \nu_m < \nu_c$		$\nu_m < \nu_a < \nu_c$				$\nu_a < \nu_c < \nu_m$			
	AG	SBO	AG		SBO		AG		SBO	
	$k=2$	$k=2$	$k=2$	General k	$k=2$	General k	$k=2$	General k	$k=2$	General k
A_*	$7.37^{+0.95}_{-0.80}$	$2.82^{+0.46}_{-0.39}$	$1.58^{+0.11}_{-0.75}$	$1.11^{+1.03}_{-0.54}$	$2.89^{+1.95}_{-1.26}$	$3.54^{+2.46}_{-1.55}$	$1.69^{+1.15}_{-0.51}$	$0.17^{+0.19}_{-0.09}$	$2.15^{+1.53}_{-0.78}$	$0.22^{+0.16}_{-0.11}$
$\eta(\eta_{\rm eff}$ for SBO)	$0.005^{+0.0004}_{-0.0004}$	$0.30^{+0.13}_{-0.12}$	$0.02^{+0.02}_{-0.01}$	$0.02^{+0.03}_{-0.02}$	$0.07^{+0.09}_{-0.05}$	$0.13^{+0.12}_{-0.07}$	$0.014^{+0.002}_{-0.002}$	$0.03^{+0.003}_{-0.003}$	$0.06^{+0.05}_{-0.03}$	$0.03^{+0.02}_{-0.01}$
ϵ_B	$0.94^{+0.05}_{-0.09}$	$0.70^{+0.20}_{-0.20}$	$0.21^{+0.24}_{-0.13}$	$0.11^{+0.17}_{-0.06}$	$0.03^{+0.03}_{-0.02}$	$0.01^{+0.01}_{-0.01}$	$0.17^{+0.14}_{-0.10}$	$0.02^{+0.01}_{-0.01}$	$0.08^{+0.09}_{-0.05}$	$0.01^{+0.01}_{-0.01}$
ϵ_e	$0.99^{+0.01}_{-0.02}$	$0.78^{+0.16}_{-0.23}$	$0.12^{+0.09}_{-0.13}$	$0.13^{+0.11}_{-0.06}$	$0.24^{+0.17}_{-0.11}$	$0.12^{+0.07}_{-0.06}$	$\cdots$	$\cdots$	$\cdots$	$\cdots$
p	$2.55^{+0.08}_{-0.06}$	$3.87^{+0.10}_{-0.19}$	$2.22^{+0.04}_{-0.04}$	$2.18^{+0.14}_{-0.09}$	$2.23^{+0.04}_{-0.05}$	$2.22^{+0.16}_{-0.13}$	$\cdots$	$\cdots$	$\cdots$	$\cdots$
k	$\cdots$	$\cdots$	$\cdots$	$1.99^{+0.01}_{-0.02}$	$\cdots$	$1.99^{+0.01}_{-0.07}$	$\cdots$	$1.91^{+0.02}_{-0.01}$	$\cdots$	$1.92^{+0.02}_{-0.02}$
s	$\cdots$	$0.55^{+0.04}_{-0.04}$	$\cdots$	$\cdots$	$0.13^{+0.08}_{-0.07}$	$0.15^{+0.08}_{-0.08}$	$\cdots$	$\cdots$	$0.35^{+0.13}_{-0.16}$	$0.08^{+0.16}_{-0.18}$
	$\chi^2_\nu = 7.55$	$\chi^2_\nu = 2.58$	$\chi^2_\nu = 1.74$	$\chi^2_\nu = 1.80$	$\chi^2_\nu = 1.72$	$\chi^2_\nu = 1.78$	$\chi^2_\nu = 1.60$	$\chi^2_\nu = 1.52$	$\chi^2_\nu = 1.58$	$\chi^2_\nu = 1.57$

Note. Here AG is the standard isotropic afterglow model and SBO is the shock breakout model. In the case of fast cooling, the data are only in the regime of ν_a to ν_c (2 to 1/3 transition of spectra), for which we do not have p dependencies in temporal or spectral slopes. The only p dependency is in the expression of ν_a via that ratio of $G(p)$ parameter, which we have taken to be of order unity for $p \sim 2.1$. The ϵ_e dependency is also not there as ν_m is unconstrained.

than cosmological GRBs at this frequency (Figure 6). However, these values are comparable to other low-luminosity GRBs, e.g., GRB 031203 (Soderberg et al. 2004) and GRB 980425 (Kulkarni et al. 1998).

The value of A_* in the standard afterglow and the SBO models are $1.58^{+0.11}_{-0.75}$ and $2.89^{+1.95}_{-1.26}$, respectively, which, assuming a wind velocity of $1000\,\mathrm{km\,s}^{-1}$, translate to mass-loss rates of $1.58^{+0.11}_{-0.75} \times 10^{-6}$ and $2.89^{+1.95}_{-1.26} \times 10^{-6}\,M_\odot\,\mathrm{yr}^{-1}$, respectively, for the two models. The nature of the surrounding ambient medium reflects on the progenitor nature of GRBs. It is expected that the progenitors of long GRBs are massive stars (Wolf–Rayet) and in most of the cases a long GRB is associated with an SN (Kulkarni et al. 1998; Woosley & Bloom 2006). Other evidence for massive star progenitors is that the long GRBs generally have star-forming host galaxies (Zhang 2019). In such a case, one expects the association with a wind-like CBM. However, several GRBs from massive stars collapse have shown homogeneous density (Panaitescu & Kumar 2001, 2002). A constant density medium can be produced around a massive star if the wind faces a shock termination (Chevalier et al. 2004). The low-frequency observations presented here provide a unique opportunity to determine the nature of the CBM of GRB 171205A and establish that GRB 171205A exploded in a wind-like environment. At uGMRT frequencies, the optically thick to thin transition peak arises after a long period of time ($t > 100$ days) after the burst, indicating a relatively high density medium. This may be created due to a large stellar mass-loss rate or a low wind velocity. Some previous works (Crowther 2003) have shown that the large mass-loss rate for Wolf–Rayet stars are associated with large metallicity of the medium. Thus GRBs in wind medium can be potential tools for studying metallicity variation at different redshifts.

The uGMRT light curve declines as $\sim t^{-0.7}$. This indicates that there is no jet break until 3 yr. There are several explanations for the lack of jet breaks in some GRBs. In the cases of GRB 980326 and GRB 980519, Granot & van der Horst (2014) have argued that a wind medium can dilute the jet break even for highly collimated bursts. The jet break will be absent if the radio emission indeed arises from a quasi-spherical afterglow, such as

that due to SBO (Nakar & Sari 2012) or a cocoon (Nakar 2015). In the case of GRB 030329, Berger et al. (2003) have argued that radio emission may arise from two components, a narrow jet, surrounded by a wider component (e.g., a cocoon) and the radio emission is being dominated by the wider component. However, the requirement of this model is that the contribution to the radio afterglow from the narrow jet may be negligible. X-ray observations cover the period of ~ 200 days and show no indication of a jet break at least until the last detection on day ~ 70. Using $t_j > 71$ days, gives a limit $\theta_j > 1.2$ rad for the AG model and $\theta_j > 1.9$ for SBO model (Nava et al. 2007; Wang et al. 2018).

Margutti et al. (2013, and references therein) have shown that ejecta kinetic energy profiles in stripped enveloped SNe vary based on different explosion mechanisms. While stripped-envelope SNe have a steep dependence $E_K \propto (\Gamma\beta)^{-5.2}$ indicating no central engine activity, relativistic SNe, sub-energetic GRBs with SBO mechanisms are flatter with $E_K \propto (\Gamma\beta)^{-2.4}$ showing weak activity from the central engine. Canonical GRBs, on the other hand, follow $E_K \propto (\Gamma\beta)^{-0.4}$ typical of jet-driven explosions with long-lasting central engines. Our radio modeling and the relativistic treatment of Barniol Duran et al. (2013), results in $E_K \approx 1.1 \times 10^{51}$ erg and $\Gamma\beta \sim 1$. For the nonrelativistic SN component, we use values from Izzo et al. (2019), i.e., SN kinetic energy $E_K = 2.4 \times 10^{52}$ erg and ejecta velocity $55{,}000\,\mathrm{km\,s}^{-1}$. Using these values, $E_K \sim (\Gamma\beta)^{-1.9}$. While GRB 171205A is a sub-energetic GRB, it follows the energy-velocity profile somewhere between canonical GRBs and SBOs. These arguments suggest that the jet and SBO both may play an important role in the late-time afterglow emission in GRB 171205A.

Since we have radio light-curve peaks at two uGMRT frequencies, we could also estimate additional parameter evolutions. The relativistic energy under the equipartition assumption at the two epochs are $E_{\rm Eq} = 3.6 \times 10^{48}$ and 4.9×10^{48} erg (Barniol Duran et al. 2013). Thus, there is an indication of the enhancement of energy $E \propto t^{0.48}$. This along with flatter light-curve decays may also be explained if there is an energy injection from the central engine to the shock. For an injection luminosity $L(t) = L_0(t/t_0)^{-q}$, $E \propto t^{1-q}$. This implies $q = 0.52$. However, our best fits result in a much larger value of
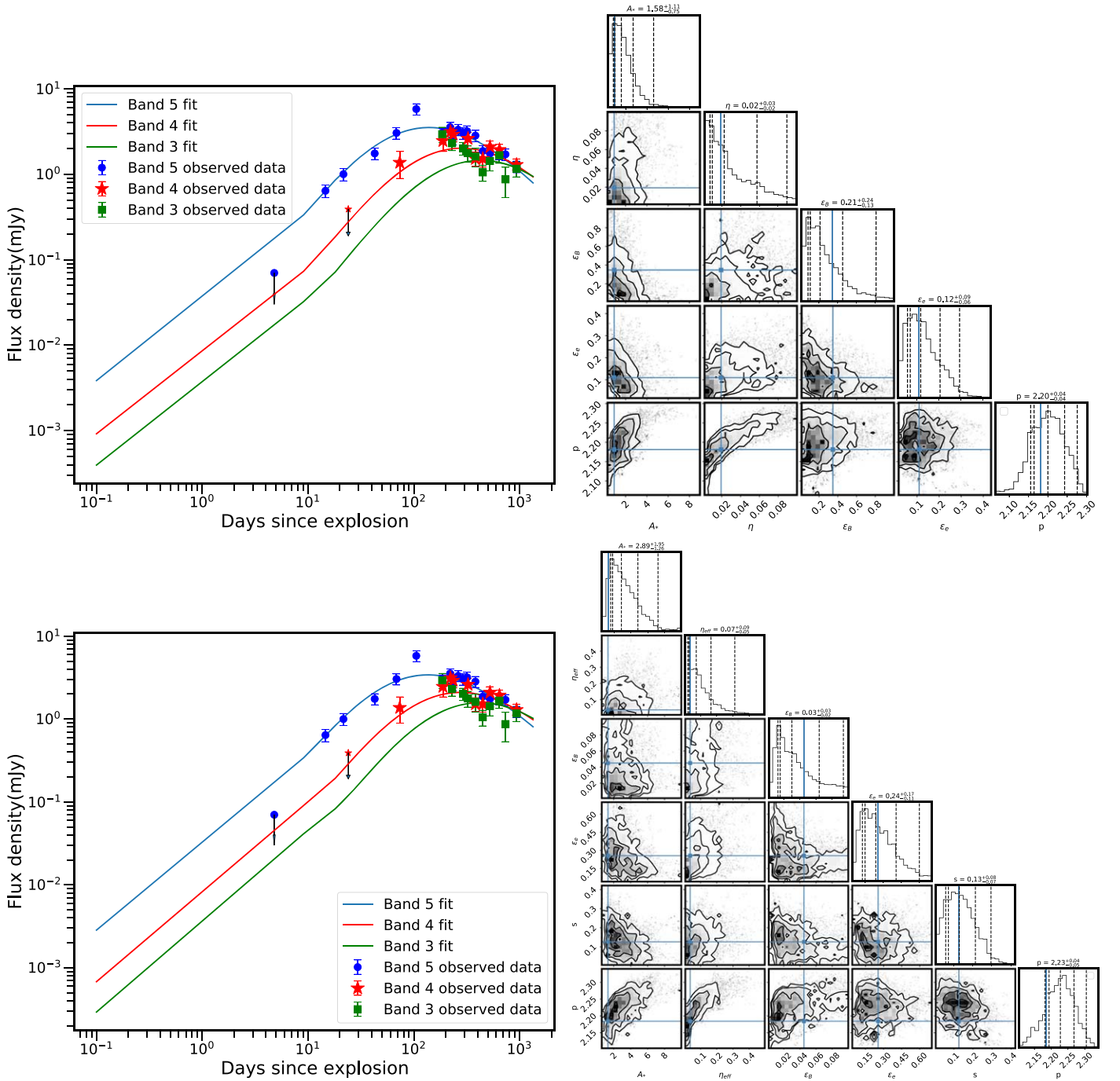
Figure 5. Upper left panel: light curves of GRB 171205A in the radio regime using the slow cooling model ($\nu_m < \nu_a < \nu_c$) and the standard wind ($k = 2$) model. Upper right panel: posterior distributions of the parameters of this model. Lower left panel: light curves of GRB 171205A in the radio regime using the slow cooling model ($\nu_m < \nu_a < \nu_c$) with the standard wind ($k = 2$) and SBO scenario. Lower right panel: posterior distributions of the parameters of this model. In the left panels, the blue, red, and green points represent the observed data in Band 5 , Band 4, and Band 3, respectively, which are included in the fit. The points with arrow only have the upper limit of flux. The lines are the best fits. In the right panels, the 2D plots show the joint probability distribution of any two parameters. The contours are at 0.5, 1, 2, and 3σ. The middle dotted lines in the 1D parameter distribution is the median value of posterior followed by 1 and 2σ lines on both sides. σ is standard deviation of the corresponding distribution.

q ($s = 0.13$, $q = 1 - s \equiv 0.87$. This may imply that if there is energy injection, it is not continuous and probably lasted for a small amount of time.

The equipartition size obtained from the above formulation (Barniol Duran et al. 2013) at the epochs of two peaks in Band 5 and Band 4 follow $R(t) \propto t^{0.49}$. We note that for the ISM and wind density profiles, R follows as $R \propto t^{1/4}$ and $R \propto t^{1/2}$, so it

also points toward a wind-like medium surrounding GRB 171205A.

Our uGMRT observations cover a period of around 1000 days. However, our data does not suggest the GRB to be in the Newtonian regime yet (Figure 4). This is not uncommon for low-luminosity GRBs (e.g., GRB 060218, Irwin & Chevalier 2016). We note that the value of $\Gamma\beta$ indicates a
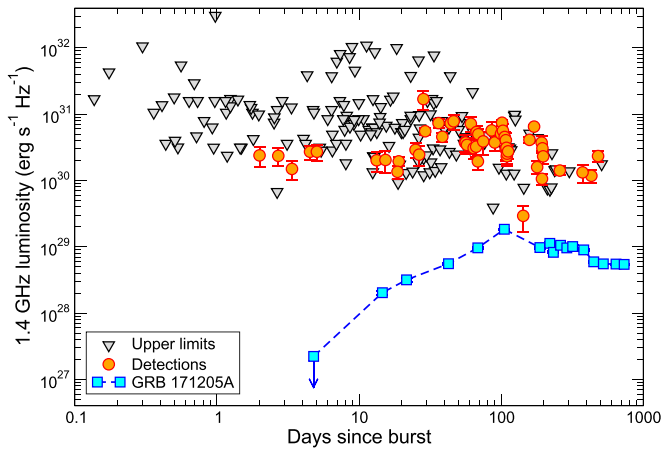
Figure 6. Plot of 1.4 GHz luminosities of canonical GRBs taken from Chandra (2016). Here we overlay the uGMRT 1.3 GHz measurements for GRB 171205A. Our values are at least two orders of magnitude smaller than canonical GRBs.

mildly relativistic outflow. Hence, it is likely that the GRB will make a transition into the Newtonian regime soon.

4.2. Shallow Decay of Radio Afterglow

We note that the decay of the radio afterglow is much shallower than that of the X-ray afterglow. The shallowness of radio light curves was first pointed out by Panaitescu & Kumar (2004). For reasonable afterglow parameters, they estimated that the afterglow is supposed to cross ν_m at around 10 days for 10 GHz and follow a decay slope of $(3p-1)/4$ for a wind medium, which was not the case for some GRBs, e.g., GRB 991216 and GRB 000926. They explored the difference between the radio and the optical decay indices, which could be caused by the fact that the injection frequency remains above the radio domain ($\sim$10 GHz), or a different population of electrons, or variability in the microparameters. Finally, they concluded that a long-lived reverse shock in the radio regime could cause this flattening. However, this is unlikely in GRB 171205A as a strong persistent reverse shock requires a low wind density (Resmi & Zhang 2016). Here the late rising of the radio afterglow suggests a comparatively high density medium, which contradicts the previous statement. So, this scenario can be excluded.

Kangas & Fruchter (2019) noted that radio afterglows of some GRBs deviate at late times and low frequencies from the standard model, and attempted to explain it with the two-component jet model, a narrow jet core and a wider cocoon surrounding the jet. Granot & Sari (2002) have explained that this flattening is due to a counter-jet, which becomes visible when turning sub-relativistic. While such two components should result in a bump, for stratified wind medium, the evolution of a counter-jet is more gradual, causing mild flattening. An energy injection event or a different component dominating the radio emission can also produce this flattening. In the case of a slightly off-axis jet, the early radio emission could possibly be from the cocoon, the accelerated polar ejecta and at a late phase the contribution from the off-axis jet coming to the line of sight can increase the total radio flux (De Colle et al. 2018). The lack of X-ray data at such late times prevents us from directly distinguishing between these scenarios.

A population of quasi-thermal electrons has also been argued as one of the reasons (Warren et al. 2017) that would mainly

dominate at radio frequencies, as it would result in an increased ν_a and suppress radio emission below this. In GRB 171205A, this has been tentatively supported from polarization measurements. According to Urata et al. (2019), the millimeter data revealed 0.27% level linear-polarization, which is a factor of 4 smaller than the optical polarization measurements. This has been explained as Faraday depolarization by non-accelerated, cool electrons in the shocked region. However, one cannot rely on these results due to the dispute of the detection claimed by Laskar et al. (2020).

4.3. Origin of Radio Emission

There have been suggestions that sub-energetic bursts are simply canonical GRBs viewed off-axis (Nakamura et al. 2001). However, such bursts will have two distinguishing characters, (a) low E_p and (b) a rise in the afterglow energy while the shocked ejecta gradually comes into the line of sight. In GRB 171205A, the afterglow energy increases slightly from 3.6×10^{48} to 4.9×10^{48} erg between $\sim$100 and $\sim$200 days. However, the E_p is comparable to that of canonical GRBs. Additionally, an off-axis jet is a geometric effect, which results in a frequency independent break in the light curve, which has not been seen for GRB 171205A, ruling out the off-axis model (D'Elia et al. 2018). Though a jet somewhat off-axis is not ruled out. D'Elia et al. (2018) found that GRB 171205A is an outlier of the Amati relation, as are some other low redshift GRBs, and its emission mechanism should be different from that of canonical, more distant GRBs.

There are two models to explain the electromagnetic emission in low-luminosity GRBs, central engine driven (Margutti et al. 2013; Irwin & Chevalier 2016) and SBO driven (Kulkarni et al. 1998; Nakar & Sari 2012; Barniol Duran et al. 2013; Suzuki & Maeda 2018). An issue with a purely SBO model is the requirement of high gamma-ray efficiency, for a quasi-spherical outflow. Another issue is the generation of such relativistic quasi-spherical outflow. One can envisage a situation where some fraction of the SN ejecta is accelerated to relativistic speeds to provide this quasi-spherical relativistic outflow. However, Tan et al. (2001) have shown that only a fraction ($\sim 10^{-4}$) of SN energy goes into relativistic ejecta. Nakar (2015) has suggested an alternative scenario where a choked jet in a low-mass envelope can put significant energy into a quasi-spherical, relativistic flow.

Our uGMRT model fits are incapable of distinguishing between canonical afterglow versus SBO AG models. We check the applicability of this model for GRB 171205A. In this model, the expanding outflow is considered to harbor a series of successive shocks, which accelerate and catch up to the boundary and hence explain the increasing afterglow energy via continuous injection. In this model, eventually the total energy should reach around 2.4×10^{52} erg (Izzo et al. 2019), the kinetic energy of the associated SN. Generally one does not see such a large amount of energy as radio observations do not cover epochs that are late enough. However, our radio observations cover a period of nearly 1000 days. The SBO model fit gives $E_K \approx 3.4 \times 10^{50}$ erg, two orders of magnitude smaller than the one predicted in the pure SBO model. Suzuki et al. (2019) carried out multiwavelength hydrodynamical modeling of GRB 171205A in the framework of the post-SBO relativistic SN ejecta–CBM interaction scenario. While they claimed that this model worked well for GRB 171205A and favor the wind model, we note some problems with their

model. They had to introduce a centrally concentrated CBM with a sudden density drop to explain the available radio and X-ray data; however, our work includes radio measurements up to 3 yr and do not show a sudden density drop.

The pure SBO model also has some other problems. An SBO model predicts a gamma-ray emission lasting $\geqslant 1000s$, lower E_p (not exceeding 50 keV), a large absorption column density, a late-time soft X-ray emission, and comparable energy in the X-ray emission and the prompt gamma-ray flare. We note that the X-ray spectrum shows an intrinsic hydrogen column density of $N_{\rm H} = 7.4^{+4.1}_{-3.6} \times 10^{20}\,{\rm cm}^{-2}$ (D'Elia et al. 2018). This intrinsic column density is at the low end of low-luminosity GRB distribution, even among low redshift Swift-XRT GRBs where the mean is $N_{\rm H} = 2.4 \times 10^{21}\,{\rm cm}^{-2}$ at $z < 0.2$ (Arcodia et al. 2016). For the observations post day 1 onwards, there may be an indication of a slightly higher column density $N_{\rm H} = 1.2^{+0.8}_{-1.7} \times 10^{21}\,{\rm cm}^{-2}$ (see footnote 2). But there is no particular indication of significant spectral softening, except a slight indication of $\Gamma = 1.63 \pm 0.30$–1.94 ± 0.23. The total X-ray energy from the first observation onwards until the last detection is at least an order of magnitude smaller than the prompt energy.

D'Elia et al. (2018) have claimed the presence of a thermal component. While SBO from SNe is the most favorable model for a thermal component (Nakar & Sari 2012; Suzuki & Maeda 2018), late-time photospheric emission from jet (Friis & Watson 2013), or thermal emission from the cocoon (Suzuki & Shigeyama 2013) can also explain this component. If we assume the blackbody component to be significant, it comprises 20% flux and has a temperature of 89 eV (D'Elia et al. 2018). This corresponds to a radius of $R = (E_{\rm iso}/aT^4_{BB})^{1/3} \approx 1.4 \times 10^{13}$ cm (a is the radiation density constant). This is much larger than the typical Wolf–Rayet star radius, but can be explained if the shock expands in a non-spherical manner. Alternatively, Nakar (2015) has suggested the presence of an optically thick stellar envelope further away from the star, from where the breakout happens.

We have seen that our observations are inconsistent with a pure SBO due to the short duration, higher E_p, shallow E versus $\Gamma\beta$ relation, low column density, and a much larger breakout radius predicted by the thermal component. It also cannot be explained as being merely a canonical GRB seen off-axis. We show below that both these components contribute toward the radio afterglow. GRB 171205A is the first GRB in which direct signatures of a cocoon have been seen (Izzo et al. 2019). This is rare because generally a line-of-sight jet is much brighter than the associated cocoon, hiding the cocoon signatures. An off-axis jet can reveal itself by the associated SN, but the cocoon signatures are long gone by the time an SN can be discovered. Ideally cocoon signatures are visible only in slightly off-axis GRBs. In GRB 171205A, the cocoon was identified by the broad absorption features overlapping the SN spectrum (Izzo et al. 2019) They also estimated, from the energy deposited in the cocoon, that the jet was quite energetic Izzo et al. (2019). This may imply that we may be seeing a slightly off-axis jet, which enabled us to reveal the cocoon, not overshadowed by the bright jet. With this knowledge, it is likely that radio afterglow arises from both components, the sub-relativistic wider cocoon and a slightly off-axis jet. The cocoon radio emission dominates the GRB emission at early times when the GRB jet is off-axis. Later the additional flux contribution comes when the jet spreads sideways and comes into the line of sight. In such a case, the total radio flux can also be large

compared to an on-axis GRBs since the cocoon and the jet carry comparable energy (De Colle et al. 2018).

Izzo et al. (2019) could not distinguish between the cocoon along with a slightly off-axis jet versus only cocoon emission, where the faint gamma-rays are the predicted signal of the cocoon breaking out of the stellar envelope. However, our radio modeling rules out the pure SBO model in favor of the cocoon along with a slightly off-axis jet. According to theoretical models, the indicated speed of the ejecta is also consistent with the sub-relativistic speeds expected in this model.

4.4. Comparison with Other Low-z Low-luminosity GRBs

With $E_{\rm iso} = 2.3 \times 10^{49}$ erg and $z = 0.0368$, GRB 171205A is one of the few low-z ($z \lesssim 0.1$), low-luminosity GRBs. Other GRBs in this category are GRB 980425, ($E_{\rm iso} = 8.5 \times 10^{47}$ erg, $z = 0.0083$; Galama et al. 1998), GRB 031203, ($E_{\rm iso} = 4.0 \times 10^{49}$ erg, $z = 0.105$; Sazonov et al. 2004), GRB 060218 ($E_{\rm iso} = 2.6 \times 10^{49}$ erg, $z = 0.033$; Campana et al. 2006), and GRB 100316D ($E_{\rm iso} = 3.7 \times 10^{49}$ erg, $z = 0.0590$; Starling et al. 2011). Like other low-luminosity GRBs, the spectrum of GRB 171205A can be fit by a simple power-law model, however, the photon index $\Gamma \sim 1.94$ is harder than these GRBs, except that of GRB 031203 ($\Gamma = 1.63$; Sazonov et al. 2004).

Even among the intrinsically sub-energetic bursts, GRB 171205A more closely resembles GRBs 980425 and 031203 and not GRBs 060218 and 100316D. GRBs 980425 and 031203 were difficult to realize in the SBO models due to their relatively hard spectra, shorter durations, and larger E_p, though a lack of thermal equilibrium may accommodate it (Katz et al. 2010). GRBs 060218 and 100316D stand out due to their large durations of a few thousand seconds and lower peak energies, $E_p < 50$ keV. The shorter T_{90} and higher $E_{\rm p}$ for GRB 171205A are comparable to the respective values for GRBs 980425 and 031203.

A major difference between GRB 171205A and other low-luminosity GRBs is the absence of intrinsic absorption column density. All other GRBs in this class show significant neutral hydrogen column density $N_{\rm H} \sim (6-7) \times 10^{21}\,{\rm cm}^{-2}$, as opposed to an order of magnitude lower $N_{\rm H}$ for GRB 171205A (D'Elia et al. 2018). The higher column density is considered an essential feature for SN SBO models in low-luminosity GRBs.

The peak radio flux density of GRB 171205A at 1.3 GHz is $\sim 10^{29}\,{\rm erg\,s}^{-1}\,{\rm Hz}^{-1}$. This value is comparable to other low-luminosity GRBs, e.g., GRB 031203 (Soderberg et al. 2004). However, the X-ray luminosity at 10 hr is $L_{\rm x} \approx 2 \times 10^{42}\,{\rm erg\,s}^{-1}$, which is four times smaller than that of GRB 031203 ($L_{\rm x} = 9 \times 10^{42}\,{\rm erg\,s}^{-1}$; Soderberg et al. 2004). This discrepancy is even more significant for a wind-like medium, since the measured peak radio luminosities are at the 1.3 and 8.5 GHz bands for GRB 171205A and GRB 031203, respectively.

It has been found that the X-ray afterglow decays slowly in low-luminosity GRBs. For example, the X-ray emission in GRB 031203 followed $F_{\rm X-ray}(t) \propto \nu^{-0.8}t^{-0.4}$ (Soderberg et al. 2004), and for GRB 980425 $F_{\rm X-ray}(t) \propto \nu^{-1}t^{-0.2}$ (Kulkarni et al. 1998). This is opposed to the canonical GRBs with $F_{\rm X-ray}(t) \propto \nu^{-1.3}t^{-1}$. Barniol Duran et al. (2015) have shown that a flat temporal decay of the X-ray light curve can be explained by the SBO model, although the dominance of an underlying SN has also been suggested as a possible reason for this flatness (Soderberg et al. 2004). With $F_{\rm X-ray}(t) \propto \nu^{-0.94}t^{-1.1}$, GRB 171205A is more like

canonical GRBs. On the contrary, the X-ray spectral index was very soft for GRB 060218A with $F_{\text{X-ray}}(t) \propto \nu^{-2.2} t^{-1.1}$, which softened even further at later epochs (Soderberg et al. 2006). GRB 171205A did not have that much spectral softening. In addition, contrary to smooth light curves of low-luminosity GRBs, the X-ray light curve of GRB 171205A revealed three temporal breaks (D'Elia et al. 2018).

The lack of jet break seems to be a common feature of low-luminosity GRBs. This may either indicate a much wider angle ejecta responsible for afterglow emission, or a stratified medium that can dilute the jet break in GRBs and hide its signatures.

Another defining feature of these GRBs is the presence of a thermal component, which has also been seen in GRB 171205A (D'Elia et al. 2018). Though this feature is quite common in GRBs associated with SNe (Campana et al. 2006; Starling et al. 2011), their origin is still a matter of debate. SBO from the relativistic SN shell is the most favorable model (Suzuki & Maeda 2018), however, late-time photospheric emission from a jet (Friis & Watson 2013), or a thermal emission from a cocoon (Suzuki & Shigeyama 2013) could also explain this component. However, it appears that the presence of a thermal component is not a unique feature of low-luminosity GRBs. Starling et al. (2012) and Sparre & Starling (2012) analyzed a sample of canonical GRBs and found evidence of a thermal component in a significant number of GRBs, though large radii associated with the blackbody emission argue against the SBO model.

Finally, while low-luminosity GRBs are considered to be a different class, Nakar (2015) has provided a unified picture of low-luminosity GRBs and cosmological GRBs, in terms of a key difference, namely, the existence of an extended low-mass envelope. In the unified model, the envelope is present in low-luminosity GRBs, but absent in cosmological GRBs. The lack of an envelope allows a jet to launch without any resistance in cosmological GRBs, but the extended envelope in low-luminosity GRBs smothers the jet and deposits a large amount of energy in the stellar envelope, driving a mildly relativistic shock producing low-luminosity GRBs via SBO. Our model does not support this picture.

5. Summary and Conclusions

In this paper, we have presented the gigahertz to sub-gigahertz observations of a low-luminosity GRB 171205A up to around 1000 days. These are the best sampled low-frequency light curves of any GRB. For the first time we report the lowest-frequency (250–500 MHz) detection of a GRB. Our light curves cover a period of 2 yr. While we are able to see the light-curve peak transitions in Bands 5 and 4, we missed the peak in Band 3 due to the lack of early data. The radio data suggest that the GRB exploded in a wind medium. At uGMRT frequencies at late time, the afterglow is in the $\nu_m < \nu_a < \nu_c$ regime, a common phenomenon seen in late-time radio afterglows. The late-time Chandra X-ray measurements constrain the jet break to be $t_{\text{jet}} > 71$ days.

Even though GRB 171205A has significant similarities to other low-luminosity GRBs, it deviates from this class in many respects. We suggest that the radio emission arises from both a cocoon and a jet, where the jet is slightly off-axis (Izzo et al. 2019). The early epoch radio emission is dominated by the cocoon surrounding the jet, while the late-time radio emission has a contribution from the jet. The flatter radio light curves,

harder GRB X-ray spectrum, large E_p, shorter T_{90}, kinetic energy—ejecta velocity relation, and time dependence of various parameters are consistent with this picture. Our work emphasizes the importance of the nature of CBM, which is critical in understanding the evolution of GRB afterglows, and are best revealed by low-frequency radio measurements.

ORCID iDs

Barun Maity (ID) https://orcid.org/0000-0002-4682-6970
Poonam Chandra (ID) https://orcid.org/0000-0002-0844-6563

References

Amati, L., Frontera, F., Tavani, M., et al. 2002, A&A, 390, 81
Arcodia, R., Campana, S., & Salvaterra, R. 2016, A&A, 590, A82
Arnaud, K. A. 1996, in ASP Conf. Ser. 101, Astronomical Data Analysis Software and Systems V, ed. G. H. Systems & J. Barnes (San Francisco, CA: ASP), 17
Barniol Duran, R., Nakar, E., & Piran, T. 2013, ApJ, 772, 78
Barniol Duran, R., Nakar, E., Piran, T., & Sari, R. 2015, MNRAS, 448, 417
Berger, E., Kulkarni, S. R., Pooley, G., et al. 2003, Natur, 426, 154
Blandford, R. D., & McKee, C. F. 1976, PhFl, 19, 1130
Bromberg, O., Nakar, E., & Piran, T. 2011, ApJL, 739, L55
Campana, S., Mangano, V., Blustin, A. J., et al. 2006, Natur, 442, 1008
Cano, Z., Izzo, L., de Ugarte Postigo, A., et al. 2017a, A&A, 605, A107
Cano, Z., Wang, S.-Q., Dai, Z.-G., & Wu, X.-F. 2017b, AdAst, 2017, 8929054
Cenko, S. B., Gal-Yam, A., Kasliwal, M. M., et al. 2013, GCN, 14998, 1
Chandra, P. 2016, AdAst, 2016, 296781
Chandra, P., Cenko, S. B., Frail, D. A., et al. 2008, ApJ, 683, 924
Chandra, P., & Kanekar, N. 2017, ApJ, 846, 111
Chandra, P., Nayana, A. J., Bhattacharya, D., Cenko, S. B., & Corsi, A. 2017a, GCN, 22264, 1
Chandra, P., Bhattacharya, D., Nayana, A. J., Cenko, S. B., & Corsi, A. 2017b, GCN, 22222, 1
Chevalier, R. A., & Li, Z.-Y. 2000, ApJ, 536, 195
Chevalier, R. A., Li, Z.-Y., & Fransson, C. 2004, ApJ, 606, 369
Crowther, P. A. 2003, in IAU Symp. 212, A Massive Star Odyssey: From Main Sequence to Supernova, ed. K. van der Hucht, A. Herrero, & C. Esteban (San Francisco, CA: ASP), 47
Daigne, F., & Mochkovitch, R. 2007, A&A, 465, 1
De Colle, F., Kumar, P., & Aguilera-Dena, D. R. 2018, ApJ, 863, 32
D'Elia, V., Campana, S., D'Aì, A., et al. 2018, A&A, 619, A66
D'Elia, V., D'Ai, A., Lien, A. Y., & Sbarufatti, B. 2017, GCN, 22177, 1
de Ugarte Postigo, A., Schulze, S., Bremer, M., et al. 2017, GCN, 22187, 1
Evans, P. A., Beardmore, A. P., Page, K. L., et al. 2007, A&A, 469, 379
Foreman-Mackey, D., Hogg, D. W., Lang, D., & Goodman, J. 2013, PASP, 125, 306
Frail, D. A., Waxman, E., & Kulkarni, S. R. 2000, ApJ, 537, 191
Friis, M., & Watson, D. 2013, ApJ, 771, 15
Fruscione, A., McDowell, J. C., Allen, G. E., et al. 2006, Proc. SPIE, 6270, 62701V
Fynbo, J. P. U., Jakobsson, P., Prochaska, J. X., et al. 2009, ApJS, 185, 526
Galama, T. J., Vreeswijk, P. M., van Paradijs, J., et al. 1998, Natur, 395, 670
Gao, H., Lei, W.-H., You, Z.-Q., & Xie, W. 2016, ApJ, 826, 141

Gao, H., Lei, W.-H., Zou, Y.-C., Wu, X. F., & Zhang, B. 2013, NewAR, 57, 141
Granot, J., & Sari, R. 2002, ApJ, 568, 820
Granot, J., & van der Horst, A. J. 2014, PASA, 31, e008
Hjorth, J., Sollerman, J., Møller, P., et al. 2003, Natur, 423, 847
Irwin, C. M., & Chevalier, R. A. 2016, MNRAS, 460, 1680
Izzo, L., de Ugarte Postigo, A., Maeda, K., et al. 2019, Natur, 565, 324
Izzo, L., Kann, D. A., Fynbo, J. P. U., Levan, A. J., & Tanvir, N. R. 2017, GCN, 22178, 1
Kangas, T., & Fruchter, A. 2019, ApJ, submitted (arXiv:1911.01938)
Katz, B., Budnik, R., & Waxman, E. 2010, ApJ, 716, 781
Kouveliotou, C., Meegan, C. A., Fishman, G. J., et al. 1993, ApJL, 413, L101
Kulkarni, S. R., Frail, D. A., Wieringa, M. H., et al. 1998, Natur, 395, 663
Laskar, T., Coppejans, D. L., Margutti, R., & Alexander, K. D. 2017, GCN, 22216, 1
Laskar, T., Hull, C. L. H., & Cortes, P. 2020, ApJ, 895, 64
Leung, J., Murphy, T., Lenc, E., Dobie, D., & Kaplan, D. 2020, GCN, 27812, 1
Longair, M. S. 2011, High Energy Astrophysics (Cambridge: Cambridge Univ. Press)
Malesani, D., Tagliaferri, G., Chincarini, G., et al. 2004, ApJL, 609, L5
Margutti, R., Soderberg, A. M., Wieringa, M. H., et al. 2013, ApJ, 778, 18
Melandri, A., Malesani, D. B., Izzo, L., et al. 2019, MNRAS, 490, 5366
Melandri, A., Pian, E., D'Elia, V., et al. 2014, A&A, 567, A29
Melandri, A., Pian, E., Ferrero, P., et al. 2012, A&A, 547, A82
Nakamura, T., Mazzali, P. A., Nomoto, K., & Iwamoto, K. 2001, ApJ, 550, 991
Nakar, E. 2015, ApJ, 807, 172
Nakar, E., & Piran, T. 2017, ApJ, 834, 28
Nakar, E., & Sari, R. 2012, ApJ, 747, 88
Nava, L., Ghisellini, G., Ghirlanda, G., et al. 2007, MNRAS, 377, 1464
Panaitescu, A., & Kumar, P. 2001, ApJ, 554, 667
Panaitescu, A., & Kumar, P. 2002, ApJ, 571, 779
Panaitescu, A., & Kumar, P. 2004, MNRAS, 350, 213
Perez-Torres, M., Cenko, S. B., Horesh, A., & Alberdi, A. 2018, GCN, 22302, 1

Perley, D. A., Schulze, S., & de Ugarte Postigo, A. 2017, GCN, 22252, 1
Perley, D. A., & Taggart, K. 2017, GCN, 22194, 1
Planck Collaboration, Ade, P. A. R., Aghanim, N., et al. 2014, A&A, 571, A16
Resmi, L., & Zhang, B. 2016, ApJ, 825, 48
Rhoads, J. E. 1999, ApJ, 525, 737
Sazonov, S. Y., Lutovinov, A. A., & Sunyaev, R. A. 2004, Natur, 430, 646
Schmidt, M. 2001, ApJ, 552, 36
Schulze, S., Malesani, D., Cucchiara, A., et al. 2014, A&A, 566, A102
Soderberg, A. M., Kulkarni, S. R., Berger, E., et al. 2004, Natur, 430, 648
Soderberg, A. M., Kulkarni, S. R., Nakar, E., et al. 2006, Natur, 442, 1014
Sparre, M., & Starling, R. L. C. 2012, MNRAS, 427, 2965
Starling, R. L. C., Page, K. L., Pe'er, A., Beardmore, A. P., & Osborne, J. P. 2012, MNRAS, 427, 2950
Starling, R. L. C., Wiersema, K., Levan, A. J., et al. 2011, MNRAS, 411, 2792
Suzuki, A., & Maeda, K. 2018, MNRAS, 478, 110
Suzuki, A., Maeda, K., & Shigeyama, T. 2017, ApJ, 834, 32
Suzuki, A., Maeda, K., & Shigeyama, T. 2019, ApJ, 870, 38
Suzuki, A., & Shigeyama, T. 2013, ApJL, 764, L12
Tan, J. C., Matzner, C. D., & McKee, C. F. 2001, ApJ, 551, 946
Taylor, G. B., Carilli, C. L., & Perley, R. A. 1999, ASP Conf. Ser. 180, Synthesis Imaging in Radio Astronomy II (San Francisco, CA: ASP)
Terreran, G., Fong, W., Margutti, R., et al. 2019, GCN, 25664, 1
Trushkin, S. A., Erkenov, A. K., Tsybulev, P. G., & Nizhelskij, N. A. 2017, GCN, 22258, 1
Urata, Y., Toma, K., Huang, K., et al. 2019, ApJL, 884, L58
van der Horst, A. J. 2007, PhD thesis, Broadband View of Blast Wave Physics: A Study of Gamma-Ray Burst Afterglows, Univ. Amsterdam
Wang, X.-G., Zhang, B., Liang, E.-W., et al. 2018, ApJ, 859, 160
Warren, D. C., Ellison, D. C., Barkov, M. V., & Nagataki, S. 2017, ApJ, 835, 248
Woosley, S., & Bloom, J. 2006, ARA&A, 44, 507
Zhang, B. 2019, The Physics of Gamma-Ray Bursts (Cambridge: Cambridge Univ. Press)
Zhang, B., Liang, E., Page, K. L., et al. 2007, ApJ, 655, 989